





Can the Superposition of Evaporative Flows Explain Broad Fe XXI Profiles during Solar Flares?

Vanessa Polito¹ , Paola Testa¹ , and Bart De Pontieu^{2,3} 

¹Harvard-Smithsonian Center for Astrophysics, 60 Garden Street, Cambridge, MA 01238, USA

²Lockheed Martin Solar & Astrophysics Lab, Org. A021S, Building 252, 3251 Hanover Street, Palo Alto, CA 94304, USA

³Rosslund Centre for Solar Physics and Institute of Theoretical Astrophysics, University of Oslo, P.O. Box 1029 Blindern, NO-0315 Oslo, Norway

Received 2019 May 10; revised 2019 June 10; accepted 2019 June 11; published 2019 July 8

Abstract

The observation of the high-temperature ($\gtrsim 10$ MK) Fe XXI 1354.1 Å line with the *Interface Region Imaging Spectrograph* has provided significant insights into the chromospheric evaporation process in flares. In particular, the line is often observed to be completely blueshifted, in contrast to previous observations at lower spatial and spectral resolution, and in agreement with predictions from theoretical models. Interestingly, the line is also observed to be mostly symmetric and significantly broader than expected from thermal motions (assuming the peak formation temperature of the ion is in equilibrium). One popular interpretation for the nonthermal broadening is the superposition of flows from different loop strands. In this work, we test this scenario by forward-modeling the Fe XXI line profile assuming different possible observational scenarios using hydrodynamic simulations of multi-thread flare loops with the 1D RADYN code. Our results indicate that the superposition of flows alone cannot easily reproduce both the symmetry and the significant broadening of the line and that some other physical process, such as turbulence, or a much larger ion temperature than previously expected, likely needs to be invoked in order to explain the observed profiles.

Key words: line: profiles – Sun: flares – Sun: UV radiation – techniques: spectroscopic

1. Introduction

Understanding the physical mechanisms responsible for flares still remains an important outstanding problem in astrophysics. One long-standing puzzle concerns the origin of large nonthermal broadenings in the profiles of blueshifted high-temperature lines observed at the footpoints of flare loops during *chromospheric evaporation*, which were first observed in X-ray spectra from highly ionized ions with *SOLFLEX* and the *Solar Maximum Mission* (e.g., Doschek et al. 1979; Mason et al. 1986). These early observations showed asymmetric line profiles characterized by a blue wing component (≈ 400 km s⁻¹) superimposed on a dominant at-rest component, in contrast with the prediction from hydrodynamic single flare-loop models of completely blueshifted lines (Emslie & Alexander 1987). Another distinctive feature of the observed spectral lines was their large nonthermal broadenings (with nonthermal velocities > 100 km s⁻¹), which are significantly larger than the thermal width estimated from the electron temperature. These observations, however, had coarse spatial resolution and were obtained by averaging large regions on the Sun.

The advent of spatially resolved spectrometers such as *SOHO/CDS* (Coronal Diagnostic Spectrometer; Harrison et al. 1995) and *Hinode/EIS* (EUV Imaging Spectrometer; Culhane et al. 2007) provided a much clearer picture of the plasma dynamics during flares (e.g., del Zanna et al. 2006; Milligan & Dennis 2009; Young et al. 2013). Nevertheless, most of the observed spectra (with a few exceptions, e.g., Del Zanna et al. 2011; Brosius 2013) still showed asymmetric lines that could be fitted with multi-Gaussian profiles, often dominated by a rest component (e.g., Doschek et al. 2015; Polito et al. 2017).

Thanks to its unprecedented spatial (0.33) and spectral resolution (down to 1–2 km s⁻¹) and fast temporal cadence (as high as 1.5 s), *Interface Region Imaging Spectrograph* (*IRIS*; De Pontieu et al. 2014) has significantly improved over the

capability of these previous spectroscopic instruments and provided exciting new insights into the understanding of chromospheric evaporation in flares. A notable example is the systematic observation of fully blueshifted profiles (without the presence of a stationary component) in the spectra of the high-temperature Fe XXI line (≈ 11 MK) during evaporation, suggesting that the emission from the footpoints and loop can now be unambiguously distinguished (e.g., Tian et al. 2014; Battaglia et al. 2015; Graham & Cauzzi 2015; Polito et al. 2015, 2016; Young et al. 2015; Dudík et al. 2016). The observed blueshifted Fe XXI spectra in individual *IRIS* pixels can also often be fitted well (with no significant residuals) with a single Gaussian component (see e.g., Figure 2 of Graham & Cauzzi 2015 and Figure 8 of Polito et al. 2016) and are very broad, with FWHM ≈ 0.8 –1 Å, or equivalently Gaussian standard deviations ≈ 0.4 Å. These values correspond to nonthermal velocities ($1/e$ line width) of ≈ 100 km s⁻¹ (e.g., Graham & Cauzzi 2015; Polito et al. 2015, 2016). We also note that the Fe XXI line cannot sometimes be unambiguously detected because of its low intensity and the presence of photospheric lines, which become intense during flares (e.g., Tian et al. 2015).

Possible causes of line broadening during flares can be grouped into three main scenarios with a different dependency on the orientation of the magnetic field: (1) superposition of flows along the line of sight (LOS) of various Doppler-shifted components from unresolved loop structures (Doschek et al. 1986; Milligan 2011); (2) Alfvén waves propagating along the magnetic field and accelerating the ions in the direction perpendicular to the magnetic field (Fletcher & Hudson 2008); and (3) isotropic broadening with the absence of a preferential direction with respect to the magnetic field. The latter scenario can include different processes such as isotropic magnetohydrodynamic (MHD) wave turbulence (e.g., Larosa & Moore 1993), opacity or pressure broadening (which, however, was ruled out by

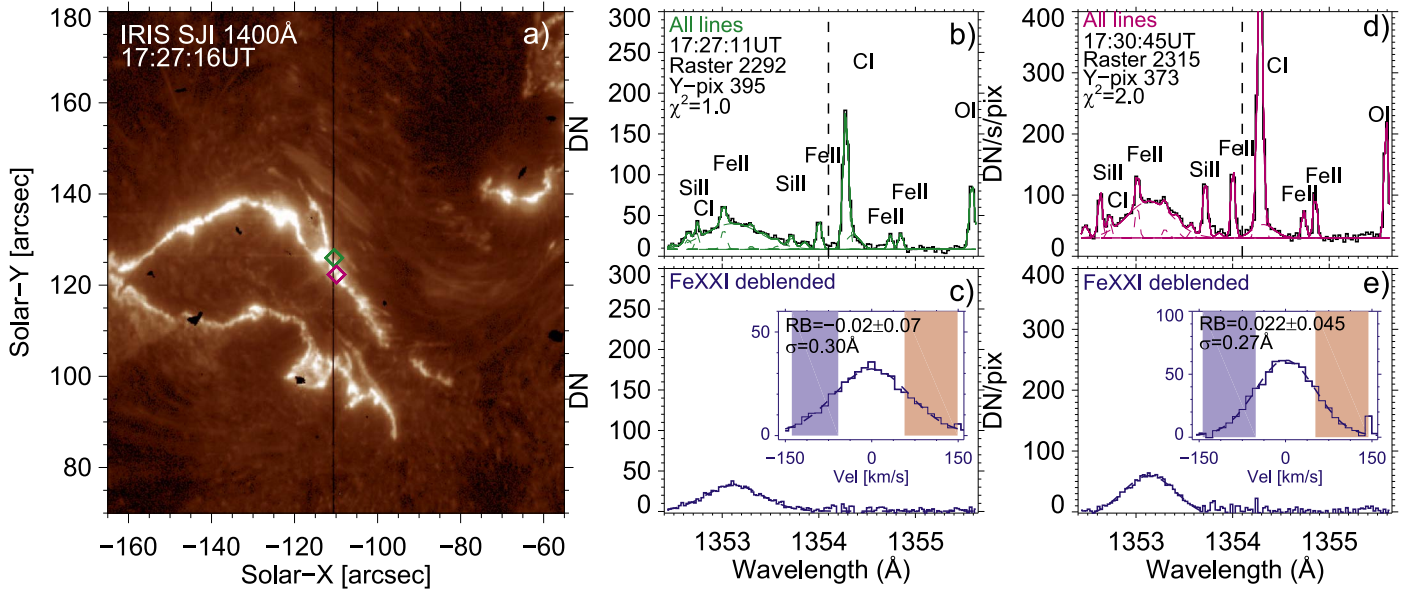


Figure 1. Broad and symmetric Fe XXI profiles in the *IRIS* 2014 September 10 flare observation. (a): SJI 1400 Å images showing the ribbons and the location of the spectrograph slit (vertical line). (b) and (d): Fe XXI spectra and narrow photospheric lines at different times and locations indicated by the corresponding colored symbols in (a). The at-rest position of Fe XXI is marked by the vertical line. (c) and (e): Fe XXI profiles after all blends have been removed. A Gaussian fit (dotted curve) is superimposed on the unblended profile. The insets illustrate the RB method for the de-blended spectra. The corresponding values of RB for a velocity interval $v_1-v_2 = 50-150 \text{ km s}^{-1}$ are shown in the insets.

Milligan 2011 as negligible), as well as very large ion temperatures (de Jager 1985). These three main scenarios carry different identifying signatures in the spectra of high-temperature lines during the evaporation, and such signatures might in principle be distinguishable in the high-resolution *IRIS* Fe XXI observations.

In this work, we investigate whether the popular superposition of flows scenario can explain the observed Fe XXI broadening and symmetry using 1D multi-thread models of evaporation in flares with the RADYN code (Carlsson & Stein 1992, 1997).

This Letter is organized as follows: Section 2 describes a typical Fe XXI *IRIS* observation that will be compared with the simulation predictions. Section 3 presents the multi-thread model, while Section 4 discusses and summarizes our findings.

2. Comparison with an Observation

Figure 1 shows the 2014 September 10 X-class flare as observed by *IRIS*. The sit-and-stare observation was spatially un-binned (X -pixel = $0''.33$, Y -pixel = $0''.166$) and with exposure time $t_{\text{exp}} \approx 8 \text{ s}$. Panel (a) shows the ribbons (which extends across $\approx 20 \times 0''.166$ *IRIS* spectrograph slit-pixels) as observed by the Slit Jaw Imager (SJI) filter centered at 1400 Å. We selected two typical broad, totally blueshifted, and sufficiently intense Fe XXI spectra, so that the line can be clearly observed above the continuum emission and any blends reliably removed (Figures 1(b)–(e)). In order to estimate the degree of symmetry of these profiles, we calculate its red–blue asymmetry (RB; following De Pontieu et al. 2009; Tian et al. 2011) as

$$\text{RB} = \frac{I_R - I_B}{I_p} \quad (1)$$

where

$$I_{R/B} = \sum_{+/-v_1}^{+/-v_2} \frac{I_p}{n_{\text{bins}}} \quad (2)$$

I_p is the de-blended line profile (after carefully subtracting the identified line blends to the observed spectrum, Figures 1(c)–(e)), $v_1 = 50 \text{ km s}^{-1}$ and $v_2 = 150 \text{ km s}^{-1}$. RB thus provides the percentage of asymmetry (blue/red-asymmetry if RB is negative/positive) of the line compared to its peak, over a certain velocity interval. The error on RB is calculated by quadratically propagating the errors associated to the numerator and denominator of Equation (1):

$$\Delta_{\text{RB}} = \text{RB} \cdot \sqrt{\left(\frac{\Delta_{(I_R - I_B)}}{I_R - I_B}\right)^2 + \left(\frac{\Delta_{I_p}}{I_p}\right)^2} \quad (3)$$

where $\Delta_{(I_R - I_B)}$ is given by the quadratic propagation of the errors on I_R and I_B (their Poisson statistical errors due to the photon noise) and the uncertainty caused by dark current subtraction and readout noise. We estimate this latter uncertainty to be around 0.95 DN per exposure by measuring the fluctuations in the background over the spectral pixels where we calculate I_R and I_B during a quiet pre-flare time interval in a region outside the flare. Further, Δ_{I_p} is given by the uncertainty in the peak estimation from the Gaussian fit. Finally, we estimate the broadening of each observed line profile by calculating its standard deviation σ . This latter was obtained by calculating the line second moment (to avoid any assumptions on the shape of the profile), and is in all cases very close to the width determined by the Gaussian fit, as shown in Figure 1.

Figure 1 shows that the broad Fe XXI profiles are mostly symmetric, with values of RB that do not exceed 0.09 (9% of the line peak) even considering the uncertainty on the RB estimation. This is in line with previous observations by Graham & Cauzzi (2015), Polito et al. (2015, 2016).

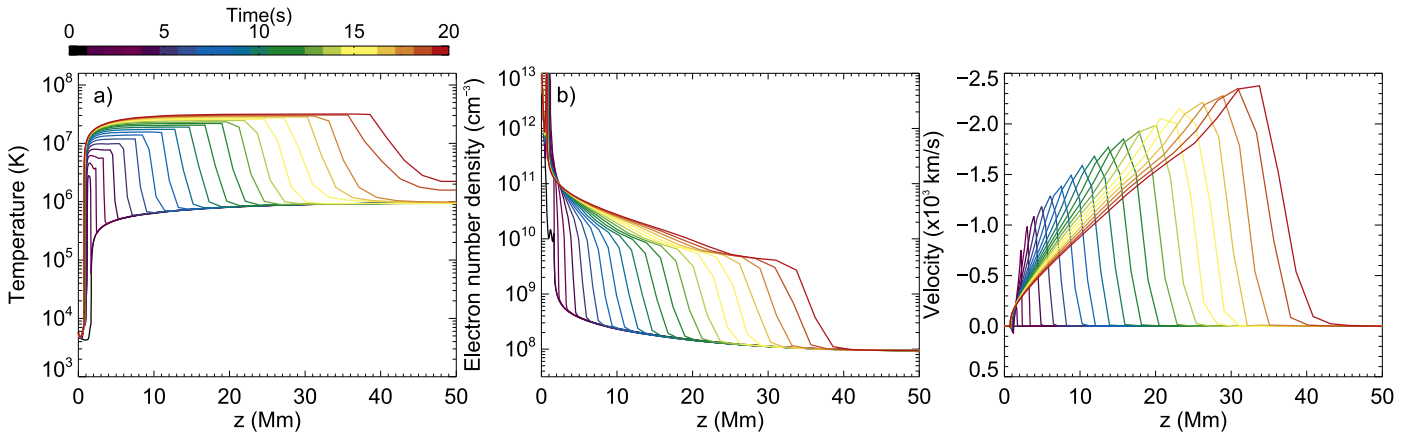


Figure 2. From left to right: evolution of the electron temperature, number density, and bulk velocity (where negative/positive indicates blue/redshifts) for the single-flare simulation.

3. Forward Modeling of Fe XXI

We perform simulations of single flare-heated loops using the RADYN code. RADYN solves the equation of charge and level population conservation coupled to the radiation hydrodynamics equation for a 1D field-aligned strand with an adaptive grid. RADYN includes non-local thermodynamic equilibrium (non-LTE) radiative transfer in the treatment of the important elements for the chromospheric energy balance (H, He, Ca II) and allows us to model heating by nonthermal electrons beams. A detailed description of the state-of-the-art RADYN code can be found in Allred et al. (2015).

We first run a single-thread flare simulation assuming a half-loop length of 50 Mm (consistent with the approximate length of the 2014 September 10 flare loops, as measured using AIA 131 Å images), with the following parameters for an electron energy power-law distribution.

1. Electron energy flux: 1.2×10^{11} ergs $\text{cm}^2 \text{s}^{-1}$ and energy cut-off E_c : 25 keV, within the range of typical values reported in previous observational and theoretical studies (see e.g., Kuridze et al. 2015; Kerr et al. 2016; Polito et al. 2016; Rubio da Costa et al. 2016; Reep et al. 2018)
2. Power-law index δ : 5, typical for large flares (e.g., Krucker et al. 2008; Hannah et al. 2011).
3. Heating duration: 60 s, based on Reep et al. (2018), who found that heating durations of ≈ 50 –100 s for each strand are needed to reproduce the observed temporal evolution of Doppler shifts during evaporation.

We assume that the loop is almost empty before the flare, with apex temperature ≈ 1 MK and density $\approx 10^8 \text{ cm}^{-3}$. Figure 2 shows the evolution of the atmospheric response along the loop (from one footpoint to the loop apex, expressed as distance in Mm above the photosphere) during the single-strand simulation. The high-energy electrons quickly deposit most of their energy in the lower atmosphere at the loop footpoints ($z \approx 1.5$ Mm) causing a rapid temperature increase and consequent overpressure that drives upflows of high-temperature plasma (> 10 MK, i.e., chromospheric evaporation). We synthesize the emission of Fe XXI using density, temperature, and bulk velocity from the simulation and atomic data from CHIANTI v8 (Del Zanna et al. 2015).

We then create a multi-strand loop model by sampling Fe XXI emission from 100 identical threads that have evolved

from 100 selected starting times (which are randomly selected, but see exceptions below) within the first 15 s of the single-loop simulation. This assumption implies that each 0.5 s time-step of our simulation represent a single state in time in the evolution of a unique strand (see e.g., Bradshaw & Klimchuk 2011). We run additional simulations by mixing loops that are heated with different energy fluxes ranging from 0.8 to 2F11, as well as repeating the same experiment with a different loop length ($L/2 = 15$ Mm), and assuming a shorter heating duration of 10 s. We found no substantial difference in the outcome of our analysis in all of these cases and therefore we only present here results for the electron beam model described above. The synthetic spectra are calculated as average data number (DN) per second for $t_{\text{exp}} = 4$ or 8 s (typical of IRIS flare observing modes).

We create several multi-thread models, which are summarized in Figure 3. Below, θ is the angle between the plane of the loops and the LOS.

1. The loops are all co-spatial (within the same pixel), with $\theta = 0^\circ$ (Figure 3(a)).
2. The loops are all co-spatial with $\theta \neq 0^\circ$ (Figure 3(b)), we choose $\theta = 30^\circ, 45^\circ$.
3. The loops are *not* co-spatial, but the location of the footpoints extend over a length $X' \approx 20 \times 0.166$ pixels (see Section 2), and $\theta = 0^\circ, 30^\circ$ or 45° (Figure 3(c)).
4. The loops are co-spatial but with different inclinations normally distributed between θ and $\theta \pm \gamma$, where $\gamma = 20^\circ$ and $\theta = 0^\circ, 30^\circ$ or 45° (Figure 3(d)).

For model 3, we consider different ways to sum the emission from the single thread.

1. The loops are activated at random times: we observe random sections of each loops at random times (*random s and t*).
2. The loops are activated progressively over time (every 0.5 s from the innermost to the outermost loop; *seq s and t*). This scenario attempts to simulate the spatial progression of footpoint brightenings along the ribbons (as described in the slipping reconnection models and seen in observations, e.g., Dudík et al. 2016).
3. Two cases in between (*random s and seq t and random t and seq s*).

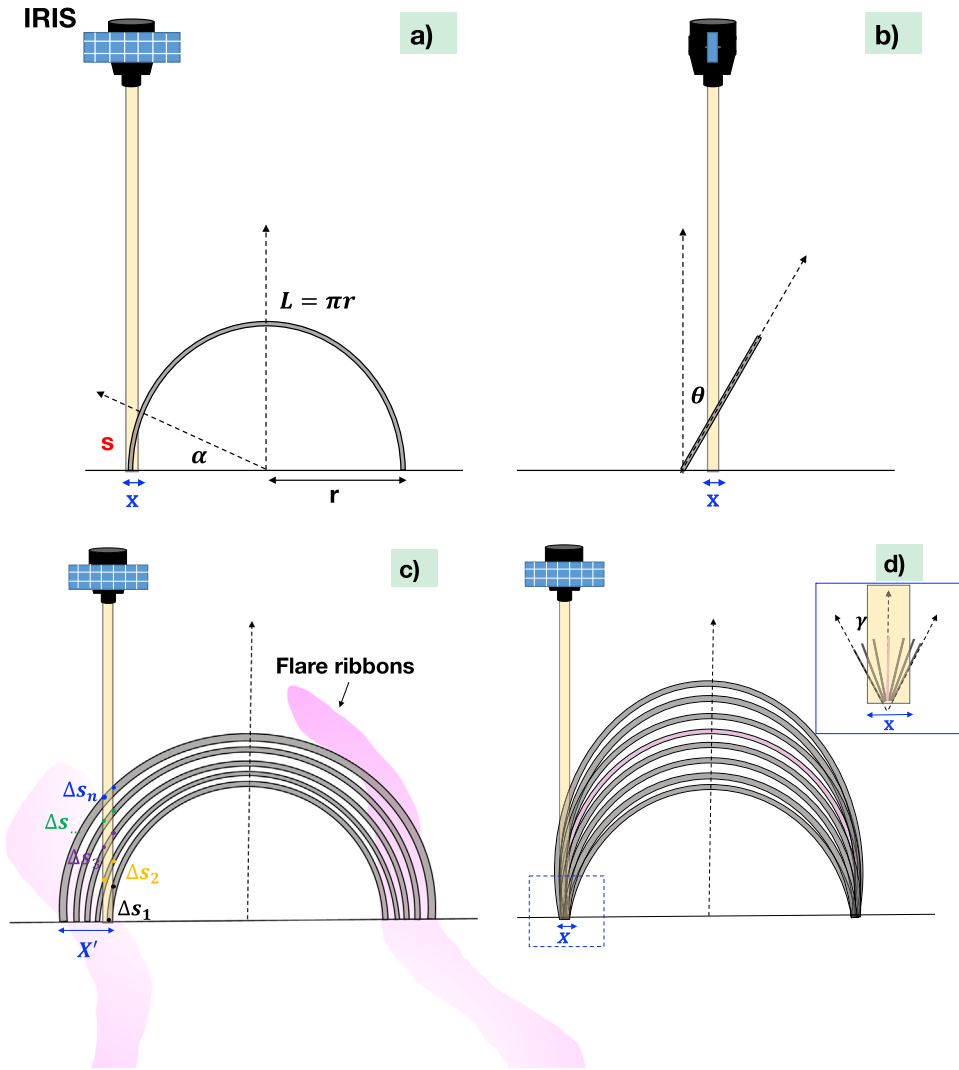


Figure 3. Cartoons illustrating different models: single-thread (or multi-thread with co-spatial loops) models with inclination angle between the plane of the loop and the LOS $\theta = 0^\circ$ (a) and $\theta \neq 0^\circ$ (b), side view); multi-thread model assuming non-co-spatial loops over a certain width X' , superposing along the LOS (c); multi-thread model with expanding loops by an angle γ (d).

For each loop, the section s that we observe within a *IRIS* pixel ($x = 0''.33$) can be calculated as follows.

1. If $\theta \leq \approx 5$ deg (Figure 3(a)) :

$$s = \alpha \cdot r \quad (4)$$

where

$$\alpha = a \arccos\left(\frac{r-x}{r}\right). \quad (5)$$

2. If $\theta > \approx 5$ deg (Figure 3(b)):

$$s = \frac{4L}{\pi} \cdot \frac{a \arcsin\left(\frac{\pi x}{4L}\right)}{\sin(\theta)}. \quad (6)$$

Figure 4(a) shows the evolution of the synthetic Fe XXI spectra for the single-loop simulation and $\theta = 0^\circ$. Panels (b) and (c) show σ and RB as a function of time, respectively. The leftmost vertical line in panel (b) indicates a minimum estimate for σ ($\approx 0.18 \text{ \AA}$, corresponding to FWHM 0.43 \AA for a Gaussian), given by the quadratic sum of the instrumental width and the thermal broadening

at the peak of the ion formation temperature in ionization equilibrium (no significant broadening in excess of this thermal width is observed during the gradual phase; Polito et al. 2015). The other vertical lines represent a range of typically observed values during the evaporation phase ($\approx 0.3\text{--}0.4 \text{ \AA}$, Graham & Cauzzi 2015; Polito et al. 2015, 2016, see also Section 1). Panel (c) also includes an error bar on the observed RB parameters (Section 2). Finally, panels (d) and (e) show synthetic Fe XXI spectra for the co-spatial multi-thread model (Model 1) and $t_{\text{exp}} 4, 8$ s. The second and third rows show similar graphs for $\theta = 30^\circ$ and 45° (Model 2). We note that the values of RB are significantly higher (approximately twice as large) than the observed ones in Figure 1 and in other *IRIS* observations (Section 1).

Figure 5 summarizes the Fe XXI synthetic spectra for the Models 3–4 discussed above. The spectra are obtained for a multi-thread loop model and different θ , analogous to the right column of Figure 4.

4. Discussion and Summary

The recent observational advances provided by *IRIS* now allow us to make major progress in understanding the cause of

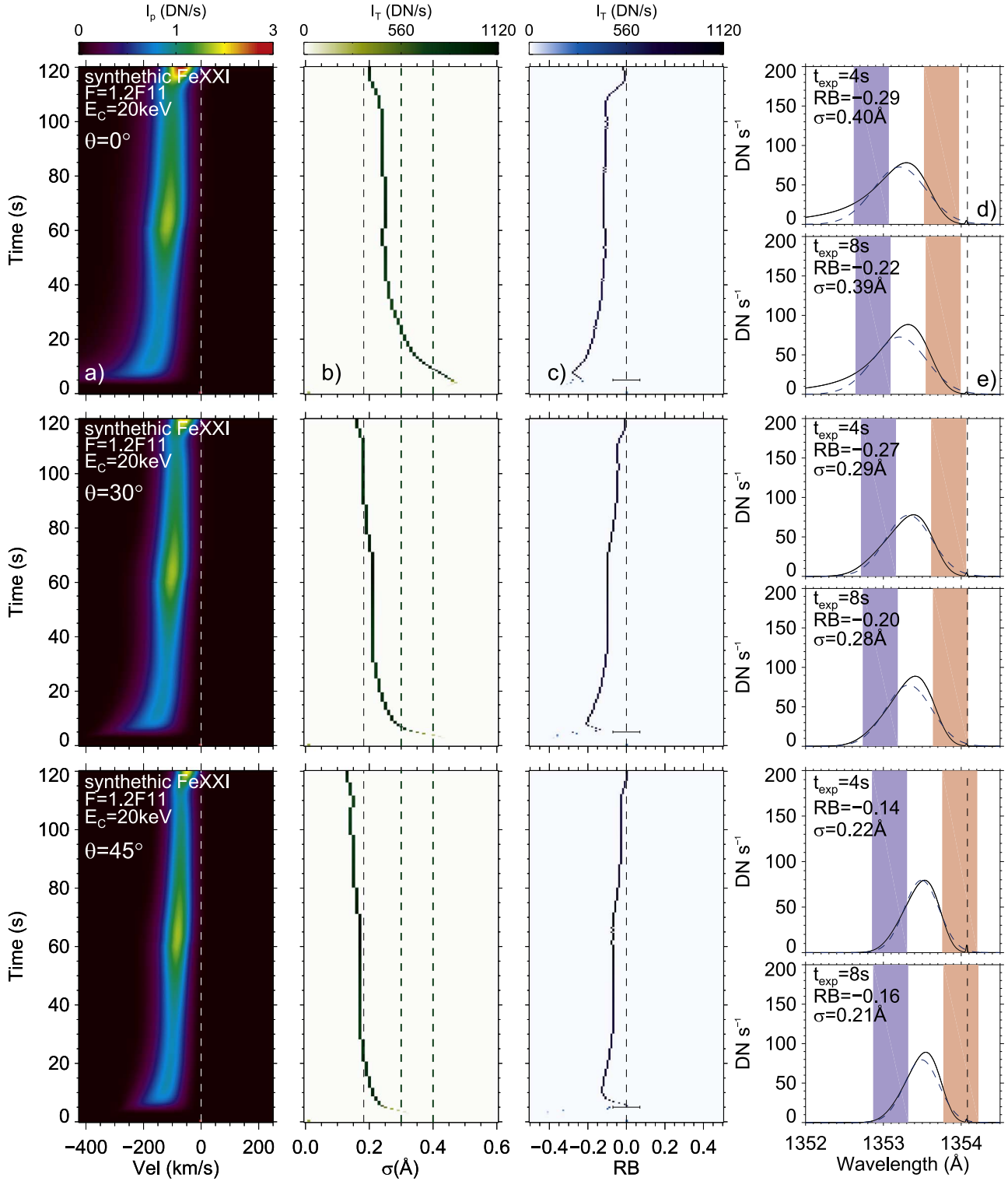


Figure 4. Synthetic spectra (a), σ (b), and RB (c) of the Fe XXI line over time for a single-thread model. The vertical lines in (b) indicate the minimum width (quadratic sum of thermal and instrumental broadening; leftmost line), and typically observed widths during chromospheric evaporation (see the text for details). (d) and (e): synthetic Fe XXI spectra (the vertical dotted line marks the rest wavelength, a Gaussian fit is overlaid) for Model 1 with $t_{\text{exp}} = 4$ and 8 s. Second and third rows: same as first row for $\theta = 30^\circ$ and 45° (Model 2).

the large nonthermal widths in the high-temperature lines. Fe XXI lines are observed to be broad, completely blueshifted, and symmetric (i.e., can be fitted with single Gaussians without significant residuals), as shown by several authors (Section 1) and also demonstrated in Section 2. We emphasize that such broadening is fundamentally different from the excess

broadenings observed in the early X-ray spectra (e.g., Antonucci et al. 1986), which were the result of plasma emission from the whole flare region. Thanks to the high resolution of *IRIS* we are now in fact isolating the high-speed upflows at the loop footpoints from the loop emission, and closely following the plasma dynamics over time. By using

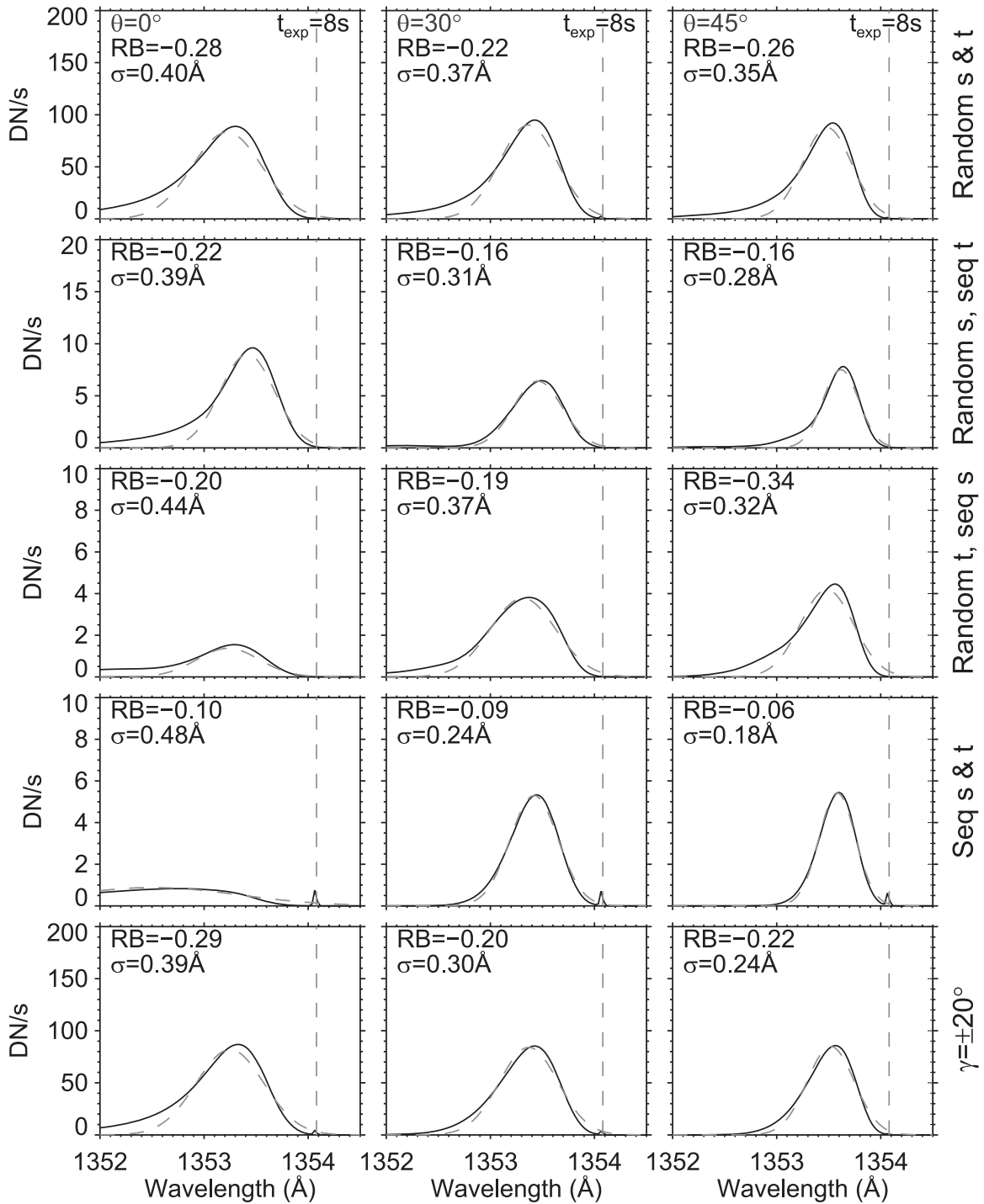


Figure 5. Synthetic Fe XXI spectra for different multi-thread models and inclination angles as indicated in the legends and the y-axis titles on the right. A single Gaussian fit is also overlaid on each spectrum.

hydrodynamic models of multi-thread flare loops with different possible geometries, we tested whether the superposition of unresolved flows within an *IRIS* pixel can reproduce the observed Fe XXI spectra. We found the following.

1. There is always an anti-correlation between broadening and symmetry: broader profiles are also more asymmetric. Narrow line profiles are in fact produced by the superposition of several upflows that have very similar velocities and are thus quite symmetric.
2. The RB asymmetry of the synthetic profiles that are sufficiently broad is significant larger ($\approx 20\%$ of the peak or more) than that of typical observed spectra ($\approx 2\%$, or up to 9%, including the errors estimate). On the other hand, more symmetric profiles (with RB values that could be compatible with the observations, within the error) can only be found in synthetic spectra whose profiles are too narrow (with $\sigma \approx 0.2 \text{ \AA}$, while observed values are at least $\approx 0.3\text{--}0.4 \text{ \AA}$, see Section 1).

We conclude that, for the models that we have explored in this work, it is difficult to produce both broad and symmetric profiles with the superposition of flows alone, and other processes, such as isotropic or Alfvén wave turbulence, may be required to explain the observations. Our findings are in agreement with Antonucci et al. (1986), who pointed out that a symmetrically broadened line profile around the line center could only be created if the flows always arrange themselves so that the contributions from up- and down-flowing material are always identical, which the authors disregarded as unlikely. Antonucci et al. (1986) also criticized the superposition of flows scenario because the degree of nonthermal excess in a large number of flares appeared to be uncorrelated with the position of flares on the solar disk (Antonucci et al. 1984). This finding was also later confirmed by a statistical study of Mariska (1994). However, these early results should be now revisited in the light of the much-improved *IRIS* resolution. Studying the dependency of the broadening and symmetry of the Fe XXI line with the direction of the magnetic field would also help us discriminate between different scenarios discussed in Section 1. Further, one might ask whether our results might be affected by the limitation of 1D codes to capture 3D structures and geometries of the lower atmospheric regions. A preliminary analysis based on *IRIS* Fe XXI 1354.1 Å synthetic spectra from a 3D MHD simulation by Cheung et al. (2019) of a flare heated by thermal conduction shows similar results to those obtained in this work, namely that the blueshifted and broad Fe XXI profiles at the flare ribbons are also mostly asymmetric. Even though these are preliminary results and will be expanded in a follow-up work, they support our results and suggest that the asymmetry of the lines does not seem to significantly depend on the exact details of the heating model or the choice of tilt angles.

The model suggested by Brannon et al. (2015), where plasma instabilities produce elliptical motion of the field lines during their reconnection, might provide yet another mechanism for creating line broadening and unresolved motions in the plasma. Nevertheless, their Si IV spectra clearly show two-component profiles due to the redshifts and blueshifts created by those motions. It is not clear how those shifts would perfectly balance each other to create symmetric Fe XXI profiles.

Finally, among possible scenarios for the excess line broadening that assume no dependency on the direction of the magnetic field (scenario 3, Section 1), a very large ion formation temperature might provide a natural explanation for a symmetric broadening of the line profiles, as suggested by (e.g., de Jager 1985) and discussed in Polito et al. (2015). Maximum values of broadening observed in Fe XXI spectra range between $\text{FWHM} \approx 0.8\text{--}1 \text{ \AA}$ (see e.g., Graham & Cauzzi 2015; Polito et al. 2015, 2016), which would be equivalent to ion temperatures of $\approx 40\text{--}60 \text{ MK}$. These values are 4–5 times above the peak formation temperature of Fe XXI in equilibrium ($\approx 11 \text{ MK}$), and still significantly larger than typically measured values of electron temperatures based on line ratios of highly ionized ions; see e.g., Del Zanna & Mason (2018). On the one hand, this is assuming that the ion and electron temperatures are the same, which is not necessarily true (e.g., Longcope & Bradshaw 2010). On the other hand, it would be difficult to maintain such a large difference between ion and electron temperatures for several minutes in a high-density plasma at the flare footpoints ($\approx 10^{11} \text{ cm}^{-3}$), see e.g., Bruner & McWhirter (1979),

Antonucci et al. (1986), and Del Zanna & Mason (2018). We note that including the effects of non-equilibrium ionization and nonthermal particle distributions may result in the ions being formed at much higher temperatures than expected (e.g., Bradshaw et al. 2004; Dudík et al. 2017; Polito et al. 2018), contributing to broadening the lines. To summarize, we speculate that both plasma turbulence (either isotropic or Alfvén wave turbulence perpendicular to the magnetic field, scenarios 2–3) and very large ion temperatures (scenario 3), could be viable mechanisms to produce symmetric and broad line profiles. More work is needed to distinguish among these possible mechanisms (or assess their relative importance). As mentioned above, crucial information could be obtained by observing the line profile properties as a function of position on the solar disk and magnetic field orientation.

These first results demonstrate the unique potential of the high-resolution *IRIS* Fe XXI line observations, whose spectral characteristics may help distinguishing between different mechanisms responsible for the large broadening of high-temperature lines and thus provide new insights into the understanding of energy transport processes in flares.

This work is supported by NASA under contract NNG09FA40C (*IRIS*). V.P. and P.T. acknowledge support by contract 8100002705 from Lockheed-Martin to SAO. We thank the anonymous referee for the useful comments. We thank Dr Alex Russell for useful discussions. *IRIS* is a NASA small explorer mission developed and operated by LMSAL with mission operations executed at NASA Ames Research center and major contributions to downlink communications funded by ESA and the Norwegian Space Centre. Resources supporting this work were provided by the NASA High-End Computing (HEC) Program (SMD-16-7704) through the NASA Advanced Supercomputing (NAS) Division at Ames Research Center. CHIANTI is a collaborative project involving researchers at the universities of Cambridge (UK), George Mason, and Michigan (USA). This Letter has benefited from discussions at the ISSI team meeting “New diagnostics of particle acceleration in solar coronal nanoflares from chromospheric observations and modeling.”

ORCID iDs

Vanessa Polito  <https://orcid.org/0000-0002-4980-7126>

Paola Testa  <https://orcid.org/0000-0002-0405-0668>

Bart De Pontieu  <https://orcid.org/0000-0002-8370-952X>

References

- Allred, J. C., Kowalski, A. F., & Carlsson, M. 2015, *ApJ*, 809, 104
 Antonucci, E., Gabriel, A. H., & Dennis, B. R. 1984, *ApJ*, 287, 917
 Antonucci, E., Rosner, R., & Tsinganos, K. 1986, *ApJ*, 301, 975
 Battaglia, M., Kleint, L., Krucker, S., & Graham, D. 2015, *ApJ*, 813, 113
 Bradshaw, S. J., Del Zanna, G., & Mason, H. E. 2004, *A&A*, 425, 287
 Bradshaw, S. J., & Klimchuk, J. A. 2011, *ApJS*, 194, 26
 Brannon, S. R., Longcope, D. W., & Qiu, J. 2015, *ApJ*, 810, 4
 Brosius, J. W. 2013, *ApJ*, 762, 133
 Bruner, E. C., Jr., & McWhirter, R. W. P. 1979, *ApJ*, 231, 557
 Carlsson, M., & Stein, R. F. 1992, *ApJL*, 397, L59
 Carlsson, M., & Stein, R. F. 1997, *ApJ*, 481, 500
 Cheung, M. C. M., Rempel, M., Chintzoglou, G., et al. 2019, *NatAs*, 3, 160
 Culhane, J. L., Harra, L. K., James, A. M., et al. 2007, *SoPh*, 243, 19
 de Jager, C. 1985, *SoPh*, 98, 267
 De Pontieu, B., McIntosh, S. W., Hansteen, V. H., & Schrijver, C. J. 2009, *ApJL*, 701, L1
 De Pontieu, B., Title, A. M., Lemen, J. R., et al. 2014, *SoPh*, 289, 2733

- del Zanna, G., Berlicki, A., Schmieder, B., & Mason, H. E. 2006, *SoPh*, **234**, 95
- Del Zanna, G., Dere, K. P., Young, P. R., Landi, E., & Mason, H. E. 2015, *A&A*, **582**, A56
- Del Zanna, G., & Mason, H. E. 2018, *LRSP*, **15**, 5
- Del Zanna, G., Mitra-Kraev, U., Bradshaw, S. J., Mason, H. E., & Asai, A. 2011, *A&A*, **526**, A1
- Doschek, G. A., Antiochos, S. K., Antonucci, E., et al. 1986, in NASA Conf. Publication 2439, *Energetic Phenomena on the Sun*, ed. M. R. Kundu & B. Woodgate (Greenbelt, MD: NASA)
- Doschek, G. A., Kreplin, R. W., & Feldman, U. 1979, *ApJL*, **233**, L157
- Doschek, G. A., Warren, H. P., Dennis, B. R., Reep, J. W., & Caspi, A. 2015, *ApJ*, **813**, 32
- Dudík, J., Dzifčáková, E., Meyer-Vernet, N., et al. 2017, *SoPh*, **292**, 100
- Dudík, J., Polito, V., Janvier, M., et al. 2016, *ApJ*, **823**, 41
- Emslie, G. A., & Alexander, D. 1987, *SoPh*, **110**, 295
- Fletcher, L., & Hudson, H. S. 2008, *ApJ*, **675**, 1645
- Graham, D. R., & Cauzzi, G. 2015, *ApJL*, **807**, L22
- Hannah, I. G., Hudson, H. S., Battaglia, M., et al. 2011, *SSRv*, **159**, 263
- Harrison, R. A., Sawyer, E. C., Carter, M. K., et al. 1995, *SoPh*, **162**, 233
- Kerr, G. S., Fletcher, L., Russell, A. J. B., & Allred, J. C. 2016, *ApJ*, **827**, 101
- Krucker, S., Battaglia, M., Cargill, P. J., et al. 2008, *A&ARv*, **16**, 155
- Kuridze, D., Mathioudakis, M., Simões, P. J. A., et al. 2015, *ApJ*, **813**, 125
- Larosa, T. N., & Moore, R. L. 1993, *ApJ*, **418**, 912
- Longcope, D. W., & Bradshaw, S. J. 2010, *ApJ*, **718**, 1491
- Mariska, J. T. 1994, *ApJ*, **434**, 756
- Mason, H. E., Shine, R. A., Gurman, J. B., & Harrison, R. A. 1986, *ApJ*, **309**, 435
- Milligan, R. O. 2011, *ApJ*, **740**, 70
- Milligan, R. O., & Dennis, B. R. 2009, *ApJ*, **699**, 968
- Polito, V., Del Zanna, G., Valori, G., et al. 2017, *A&A*, **601**, A39
- Polito, V., Dudík, J., Kašparová, J., et al. 2018, *ApJ*, **864**, 63
- Polito, V., Reep, J. W., Reeves, K. K., et al. 2016, *ApJ*, **816**, 89
- Polito, V., Reeves, K. K., Del Zanna, G., Golub, L., & Mason, H. E. 2015, *ApJ*, **803**, 84
- Reep, J. W., Polito, V., Warren, H. P., & Crump, N. A. 2018, *ApJ*, **856**, 149
- Rubio da Costa, F., Kleint, L., Petrosian, V., Liu, W., & Allred, J. C. 2016, *ApJ*, **827**, 38
- Tian, H., Li, G., Reeves, K. K., et al. 2014, *ApJL*, **797**, L14
- Tian, H., McIntosh, S. W., De Pontieu, B., et al. 2011, *ApJ*, **738**, 18
- Tian, H., Young, P. R., Reeves, K. K., et al. 2015, *ApJ*, **811**, 139
- Young, P. R., Doschek, G. A., Warren, H. P., & Hara, H. 2013, *ApJ*, **766**, 127
- Young, P. R., Tian, H., & Jaeggli, S. 2015, *ApJ*, **799**, 218